

Mesoporous Single-Crystal High-Entropy Alloy

Ravi Nandan,^a Ho Ngoc Nam,^{b} Quan Manh Phung,^{c,d} Hiroki Nara,^e Joel Henzie,^{a*} and*

Yusuke Yamauchi^{a,b,f,}*

^a Research Center for Materials Nanoarchitectonics, National Institute for Materials Science (NIMS), 1-1 Namiki, Tsukuba, Ibaraki 305-0044, Japan.

^b Department of Materials Process Engineering, Graduate School of Engineering, Nagoya University, Furo-cho, Chikusa-ku, Nagoya 464-8603, Japan.

^c Department of Chemistry, Graduate School of Science, Nagoya University, Furo-cho, Chikusa-ku, Nagoya 464-8602, Japan.

^d Institute of Transformative Bio-Molecules (WPI-ITbM), Nagoya University, Furo-cho, Chikusa-ku, Nagoya 464-8601, Japan.

^e Waseda Research Institute for Science and Engineering, Waseda University, 3-4-1 Okubo, Shinjuku, Tokyo 169-8555, Japan.

^f School of Chemical Engineering and Australian Institute for Bioengineering and Nanotechnology (AIBN), The University of Queensland, Brisbane, QLD 4072, Australia.

Corresponding Author

Email: HENZIE.Joeladam@nims.go.jp (Joel Henzie, orcid.org/0000-0002-9190-2645)

Email: honam@nagoya-u.jp (Ho Ngoc Nam, orcid.org/0000-0001-9785-5061)

Email: y.yamauchi@uq.edu.au (Yusuke Yamauchi, orcid.org/0000-0001-7854-927X)

ABSTRACT

Mesoporous high-entropy alloys (HEAs) represent a promising advancement in mesoporous metal, showing great potential for various applications. Their unique multimetallic uniformity, strong structural features, and high surface-active site exposure contribute to their practical catalytic ability. The catalytic efficiency of metal nanostructures depends on both their elemental compositions and crystallinity, with single-crystalline structures generally outperforming polycrystalline ones. However, synthesizing single-crystalline HEA nanostructures with defined mesoporosity remains challenging due to the complex fabrication process. This study introduces a block copolymer micelle-assisted soft-chemical strategy to create single-crystalline mesoporous HEAs (SCPHEAs). These structures feature uniformly sized mesopores that permeate throughout, maximizing the exposure of high-entropy alloy active sites, enhancing material utilization, and facilitating efficient mass and charge transport. The optimized SCPHEAs exhibit excellent electrocatalytic performance in methanol oxidation reactions, surpassing polycrystalline mesoporous HEAs, commercial Pt-C, and various recently reported precious metal-based HEAs and conventional alloy electrocatalysts. This superior performance is attributed to a synergistic effect that results from surface charge redistribution among different atomic entities, which enhances the adsorption of methanol and water molecules and mitigates intermediate CO poisoning. Our synthesis method enables the designing of a wide range of mesoporous HEAs with controllable morphology and crystallinity tailored for various catalytic applications and beyond.

KEYWORDS: Single crystal; High entropy alloys; Mesoporous nanostructure; Methanol Electro-oxidation; CO poisoning tolerance.

Advancements in the design of porous materials have revolutionized the development of highly efficient nanomaterials for diverse applications, including biomedicine, photonics, sensing, catalysis, and energy storage/conversion.^{1–8} The performance of these materials, especially in catalytic and electrocatalytic processes, is strongly influenced by their compositions.^{9,10} Multimetallic systems, in particular, have been shown to outperform their monometallic counterparts in complex reactions involving multiple electron transfer steps and requiring various catalytically active sites.^{10–16} High entropy alloys (HEAs), composed of five or more constituent elements, have garnered significant attention due to their vast compositional and configurational possibilities,^{17–32} offering a wide range of catalytically active sites.^{27,31}

Beyond elemental composition, nanomaterials' physical and chemical properties are profoundly affected by their crystalline nature.³² Single-crystalline systems, in particular, often exhibit superior electrical, magnetic, mechanical, and optical properties compared to their polycrystalline counterparts.^{33–39} In catalysis, the crystalline quality of the catalyst plays a critical role in exposing catalytically active sites and ensuring long-term stability. Previous studies have demonstrated the successful synthesis of single-crystalline nanomaterials, such as Ir-doped CuPd nanostructures for selective C–C bond cleavage in ethylene glycol oxidation,^{4,40} and Pt nanostars with exceptional catalytic activity toward ferricyanide reduction.⁴¹ Thus, developing synthesis protocols to engineer single-crystalline HEA nanostructures holds great promise for unlocking the full potential of HEAs, giving new insights into the composition-function correlation in complex systems like HEAs.

Despite advancements in HEA synthesis, most existing methods, including polymeric-based soft templating techniques, have mainly produced polycrystalline HEA

1 nanostructures.^{19,22,25,28,29,42} Achieving single-crystalline HEAs remains a significant
2 challenge due to the complex involvement of five or more atomic species with different
3 reduction kinetics. Incorporating mesoporosity into single-crystalline HEAs further
4 complicates the design process. However, the benefits of mesoporous structures are
5 remarkable. They provide increased exposure to active surface sites, enhance mass
6 transport, and offer synergistic effects from crystallinity engineering, which can
7 significantly enhance the overall performance of these advanced materials. Therefore,
8 this work aims to address these challenges by introducing novel approaches for creating
9 single-crystalline mesoporous HEAs. Specifically, we present an upgraded method of
10 micelle-assisted, all-wet, soft-chemical synthesis for designing single-crystal high-
11 entropy alloys (SCHEAs) (see Figure 1) from the elemental combination of Pt, Pd, Ru,
12 Ir, and Rh. Beyond the remarkable catalytic activity of platinum group metals, these
13 elements are characterized by similar atomic radii and low heat of formation, possibly
14 promoting the formation of a stable HEA structure. Additionally, their high standard
15 electrode potentials potentially reduce the risk of oxidation, ensuring durability and
16 stability for catalytic applications.²⁷ The resulting SCHEAs exhibit well-defined
17 mesopores that permeate the entire structure, enhancing mass and charge transport,
18 providing a highly active surface area, and ensuring the extensive exposure of high-
19 entropy electroactive sites. Through comprehensive experimentation with a careful
20 selection of precursor compositions and optimization of experimental conditions
21 (temperature and time), we demonstrate precise tuning of the crystallinity of PtPdRuIrRh
22 HEAs. The optimized SC-HEA achieves a mass activity of 2.7 A/mg_{Pt} and exceptional
23 stability (~93% activity retention after 2500 cycles), outperforming its polycrystalline
24 porous HEA counterpart (1.6 A/mg_{Pt}), commercially available Pt-C (0.6 A/mg_{Pt}), and

several recently reported Pt-based alloys and HEAs in methanol electro-oxidation reactions. This work provides a robust platform for crystallinity engineering, underscoring the significant potential of single-crystal HEA systems. It also offers a critical foundation for advancing future mesoporous single-crystal metals, including HEAs with more than five constituent elements, for diverse applications beyond (electro)catalysis.

RESULTS AND DISCUSSION

Structural Studies of Porous HEA Nanostructures

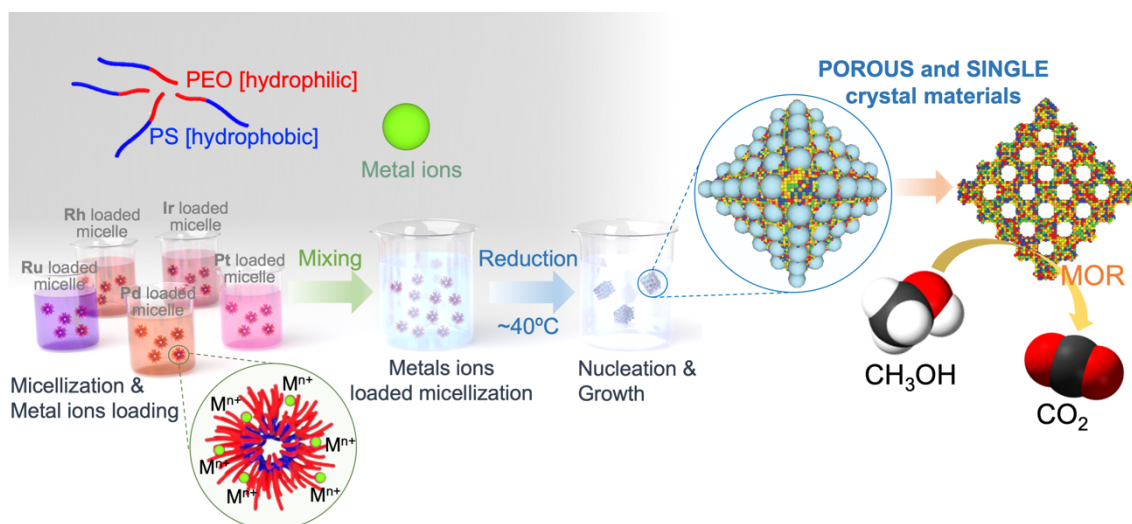


Figure 1. Schematic representation of synthesis methodology used for designing single crystal porous high entropy PtPdRuIrRh nanoalloys.

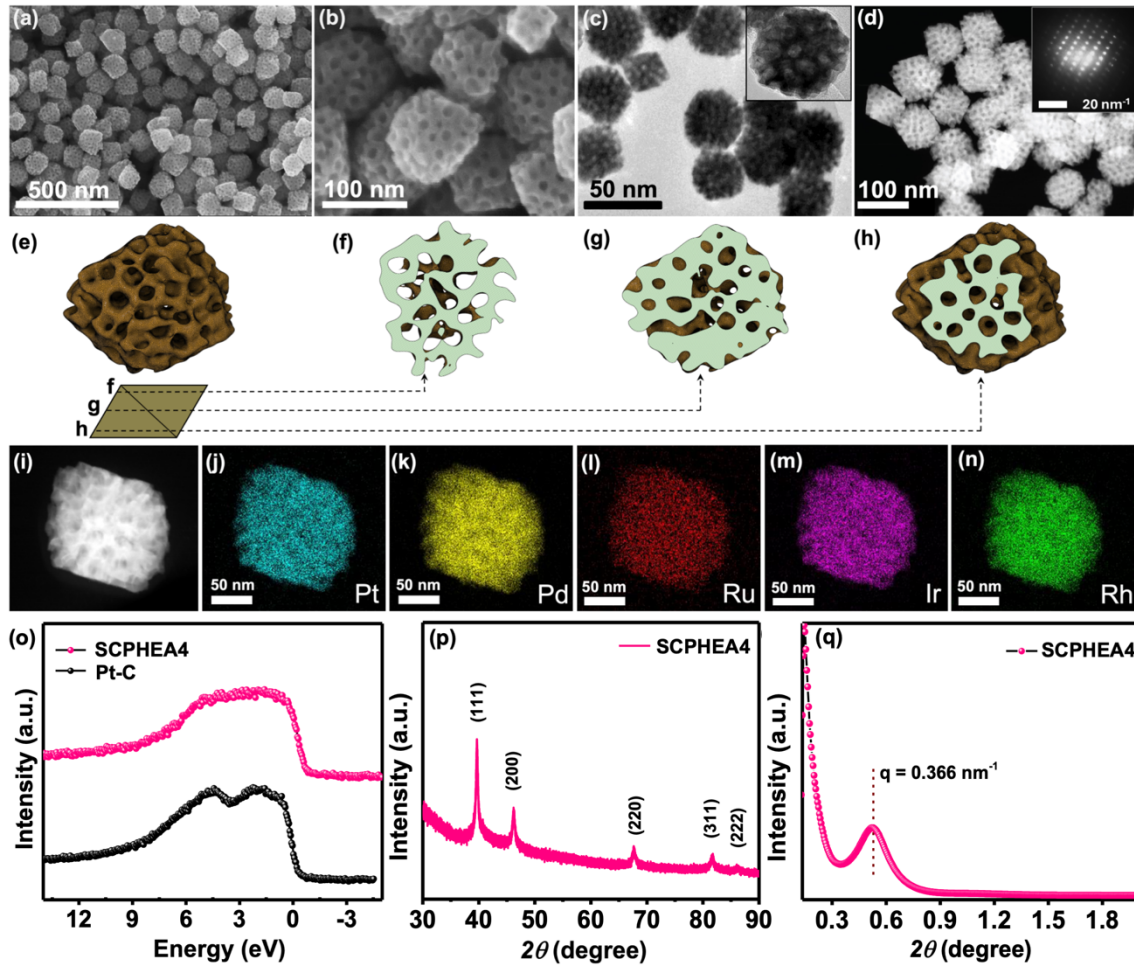
Figure 1 illustrates the synthetic process for SC-HEAs composed of PtPdRuIrRh. Initially, a diblock copolymer, polystyrene-block-polyethylene oxide (PS-b-PEO), was dissolved into *N,N*-dimethylformamide (DMF) to form a transparent solution. Aqueous metal salt solutions containing ion precursors were then gently introduced, prompting the

micellization of PS-*b*-PEO. In this process, the hydrophobic PS forms the core, while the hydrophilic PEO constitutes the exterior. Micelle formation was confirmed through the Tyndall effect (Figure S1).⁴³ The hydrophilic PEO exterior of the micelles provides a tailored microenvironment for metal ion complexation via electrostatic interactions or hydrogen bonding, depending on the coordination sphere of the metal ions.^{14,44–46} These interactions significantly reduce ion mobility, thereby decoupling their reduction behavior from standard electrochemical potentials resulting in redox kinetics governed by the local chemical environment. Consequently, the choice of copolymer is crucial. This interaction was further validated by UV-visible (UV-Vis) absorption spectra, showing a hyperchromic effect—an upward shift in absorbance—without altering peak positions compared to metal ion solutions in the absence of micelles (Figure S2).¹⁴ Sulfuric acid (H₂SO₄) was used to modulate the reducing strength of the reducing agent during the synthesis.^{13,43} The reaction mixture was then heated in a preheated oil bath at 40 °C for varying reaction durations. Following synthesis, the PtPdRuIrRh HEAs were collected via centrifugation, and the polymeric micelles were carefully removed through multiple washing steps. The single-crystalline mesoporous HEA and polycrystalline mesoporous HEA were designated as SCPHEA t and PCPHEA t , respectively, where t denotes the reaction time (in hours).

Representative scanning electron microscopic (SEM) images (Figure 2a, b) exhibit rich mesoporous features in SCPHEA4. This mesoporous structure is further evident in bright field transmission electron microscopic (TEM) images (Figure 2c) and high-angle annular dark-field scanning TEM (HAADF-STEM) images (Figure 2d). The three-dimensional (3D) tomography study reveals that these mesopores run throughout the body of the particle (Supporting video). Based on tomographic observation, the 3D reconstructed

image of single particles along their different cross-sections (Figure 2e-h) reveals that the mesoporous network is continuously distributed throughout the entire particle. This benefits mass and charge transportation and ensures the exposure and accessibility of numerous high-entropy active sites. Surprisingly, the selected area diffraction patterns (SAED, inset of Figure 2d and Figure S3) of the SCPHEA4 particle consist of clear and intense bright spots without any randomization of the diffraction spots, indicating the single-crystalline nature.^{32,47} The formation of single crystals suggests that all five elements are uniformly distributed and crystallized in a single phase. From a theoretical standpoint, this is facilitated by the small difference in the atomic radii ($\delta = 2.6\%$) of the constituent elements, which minimizes lattice strain and promotes solid-solution formation with homogeneous distribution. In this system, the configurational mixing entropy ($\Delta S_{\text{mix}}T_{\text{m}}$) significantly outweighs the mixing enthalpy (ΔH_{mix}) (i.e., $\Omega = 1.88$, where $\Omega \sim \Delta S_{\text{mix}}T_{\text{m}}/\Delta H_{\text{mix}}$), fostering a stable, well-mixed solid solution. Under suitably controlled conditions, Pt atoms became rich in content owing to their favorable redox potential and can act as primary nucleation sites to favor the growth of a single dominant face-centered cubic (fcc) or body-centered cubic (bcc) crystal rather than multiple grains. Our first-principles calculations also predict a preference for fcc phase formation over bcc, with a lattice constant of 0.390 nm (Fig. S4). Indeed, all experimental probing methods from elemental dispersive spectroscopy (EDS) in HAADF-STEM mode (Figure 2i-n), line scans (Figure S5, S6) to inductively coupled plasma optical emission spectrometry (ICP-OES, Table S1) studies confirm that Pt, Pd, Ru, Ir, and Rh are uniformly distributed throughout the SCPHEA4 nanostructure. The atomic ratio of Pt/Pd/Rh/Ru/Ir in SCPHEA4 was determined to be 63/23/9.8/1.8/2.4 by ICP-OES (Table S1) corresponding to a mixing configuration entropy value $\Delta S_{\text{mix}} \sim 1.01R$ suggesting

1 entropy entropy-stabilized system.⁴⁸



2
3 **Figure 2.** Electron microscopic and spectroscopic analyses of SCPHEA4. The
4 representative (a,b) SEM, (c) TEM, and (d) HAADF-STEM images of SCPHEA4. The
5 inset shows the SAED pattern of SCPHEA4. STEM tomography of a single SCPHEA4
6 nanoparticle, (e) rendering of the entire particle and (f-h) different cross-sections of the
7 nanoparticle, (i) HAADF-STEM image of SCPHEA4 nanoparticle subjected to EDS
8 mapping, (j-n) corresponding elemental distribution patterns of Pt, Pd, Ru Ir, and Rh,
9 respectively. (o) The valence band spectra of SCPHEA4 and Pt. (p,q) XRD and SAXS
10 patterns of SCPHEA4 nanostructures. The scattering vector for SAXS is given by $q = 4\pi$
11 $\sin\theta/\lambda$, where λ is the wavelength of X-ray radiation used.

X-ray photoelectron spectroscopy (XPS) was employed to probe the surface chemical state of SCPHEA4. Several intense peaks of Pt, Pd, Ru, Ir, and Rh indicate the multi-elemental character (Figure S7). A negative shift of approximately 0.5 eV in the Pt core spectrum for SCPHEA4, compared to the monometallic Pt system (Figure S7), is attributed to the interatomic interaction of Pt with neighboring heteroatoms (Pd, Ru, Ir, and Rh),^{28,49,50} resulting in effective electron transfer to the Pt centers. The negative shift in the Pt spectrum can be ascribed to the high electronegativity of Pt, which drives the inherent electron-withdrawing tendency of Pt during interatomic interactions with neighboring atoms in systems like HEAs.⁵¹ The increase in electron density may result in a downward shift in the *d*-band center, effectively regulating the adsorption/desorption energies of reactant and intermediate species and making Pt-based HEA systems more effective for multi-electron transfer reactions and intermediate steps like the methanol oxidation reaction (MOR).^{17,28,52,53} Hard X-ray photoelectron spectroscopy (HAXPES, Cr K α source) was employed to unveil the electronic structure modification of the SCPHEA4 exterior (Figure 2o). The featureless valence band (VB) spectrum in SCPHEA4, a common feature in HEA systems, contrasts with that of monometallic Pt systems, which exhibit distinct peaks. This reflects the overall electronic structure modification arising from complex interatomic interactions and orbital hybridization in HEAs.^{49,54} The presence of characteristic peaks in the powder X-ray diffraction (XRD) pattern is identical to that of Pt (JCPDS card No. 03-065-2868), indicating that SCPHEA4 indeed crystallizes in the fcc crystal system (Figure 2p). The lattice constant deduced from the XRD pattern for SCPHEA4 was found to be 0.392 nm, consistent with our previous theoretical prediction. This larger lattice constant compared to the individual constituent elements Rh (0.380 nm), Ir (0.383 nm), Ru (0.271 nm), Pd (0.385 nm), and Pt (0.391 nm)

can be attributed to lattice distortion due to entropy-driven phase purity, where multiple atomic species with differing sizes reside in one unit cell.^{17,28} Small-angle X-ray scattering (SAXS) pattern was recorded to probe the pore periodicity in the mesoporous structure of SCPHEA4, although the mesopore size is uniform, their arrangement is random. Unlike ordered mesoporous materials, such as those with a 2D hexagonal structure, the peak in this study is indicative of the pore-to-pore distance since uniformly sized mesopores are closely packed with each other. For SCPHEA4, the peak observed in SAXS pattern at $q = 0.366 \text{ nm}^{-1}$ (Figure 2q), corresponding to an average pore-to-pore distance of approximately 17 nm. The overall morphological and structural studies support a successful soft-templating method in which the micelles create a single-crystal mesoporous architecture consisting of Pt, Pd, Ru, Ir, and Rh elements.

Morphological and Structural Optimization Studies

To examine the effects of precursor materials and reaction conditions on the structural-morphological evolution and final crystallinity of PtPdRuIrRh HEA nanostructures, a series of controlled experiments were conducted. By systematically varying the temperature (Figure S8), type of copolymers (Figure S9), and type of acid (H_2SO_4 or HCl, Figure S10) used to regulate the reducing power of formic acid during synthesis, we identified the optimal conditions for synthesizing single-crystal porous HEA nanostructures. The $\text{PS}_{5k}\text{-}b\text{-PEO}_{2.5k}$ copolymers, H_2SO_4 acid, and a reaction temperature of 40 °C were found to be particularly effective in achieving the desired single-crystal porous HEA nanostructures of PtPdRuIrRh (details in SI).

Subsequently, a time-dependent study for SCPHEA t ($t = 1, 2$, and 6 hours) was employed to monitor the overall structure evolution/growth (Figure 3). Figures 3a and b present

representative SEM and HHADF-STEM images of the porous single crystal HEA nanostructures of PtPdRuIrRh for a reaction time of 1 hour (SCPHEA1, avg. size $\sim 40 \pm 5$ nm). The formation of single crystal can be understood by the virtue that upon mixing and initiating the reduction, the metal-ion-loaded micelles undergo aggregation, leading to localized regions of high metal ion concentration. Creating confined, chemically distinct microenvironments that promote co-reduction and discourage phase separation. This spatial constraint, combined with the influence of coordination environments, surface energies, and organic additives,¹³ facilitates non-equilibrium mixing and kinetically bypasses miscibility limitations. The resulting entropy-stabilized alloy formation is evidenced by the featureless valence band spectrum indicating a homogeneous distribution of elements and single-phase stabilization (Figures S11 and S12). The SAED pattern (Figure 3c) comprised well-defined, intense bright spots without azimuthal randomization, indicative of the characteristic single crystalline nature.⁴⁷ This is further evident in high-resolution TEM (HRTEM) images (Figure 3d and Figure S11) of SCPHEA1 nanostructure, which shows the seamless crystalline porous nanostructure comprised of (111) set of planes with an interplanar spacing of 0.22 nm (Figure 3e). EDS in HAADF-STEM mode for elemental portioning of SCPHEA1 shows a uniform distribution of elements Pt/Pd/Ru/Ir/Rh (Figure 3f) throughout the nanostructure. This is further evident from the elemental distribution profile deduced from EDS elemental portioning (Figure S12). As the reaction time increased to 2 and 4 hours, the overall size of the nanostructures grew to 60 ± 5 and $\sim 90 \pm 5$ nm, respectively, as evidenced by SEM and HAADF-STEM images (Figure 3g, h, Figure S13 (HRTEM) and Figure 2). Notably, the single-crystalline nature and elemental composition of SCPHEA2 (Figure 3g-I, Figure

S13) and SCPHEA4 (Figure 2) remained consistent with SCPHEA1 (Figure 3a-f). The atomic content of the constituting elements remains nearly constant (Table S1).

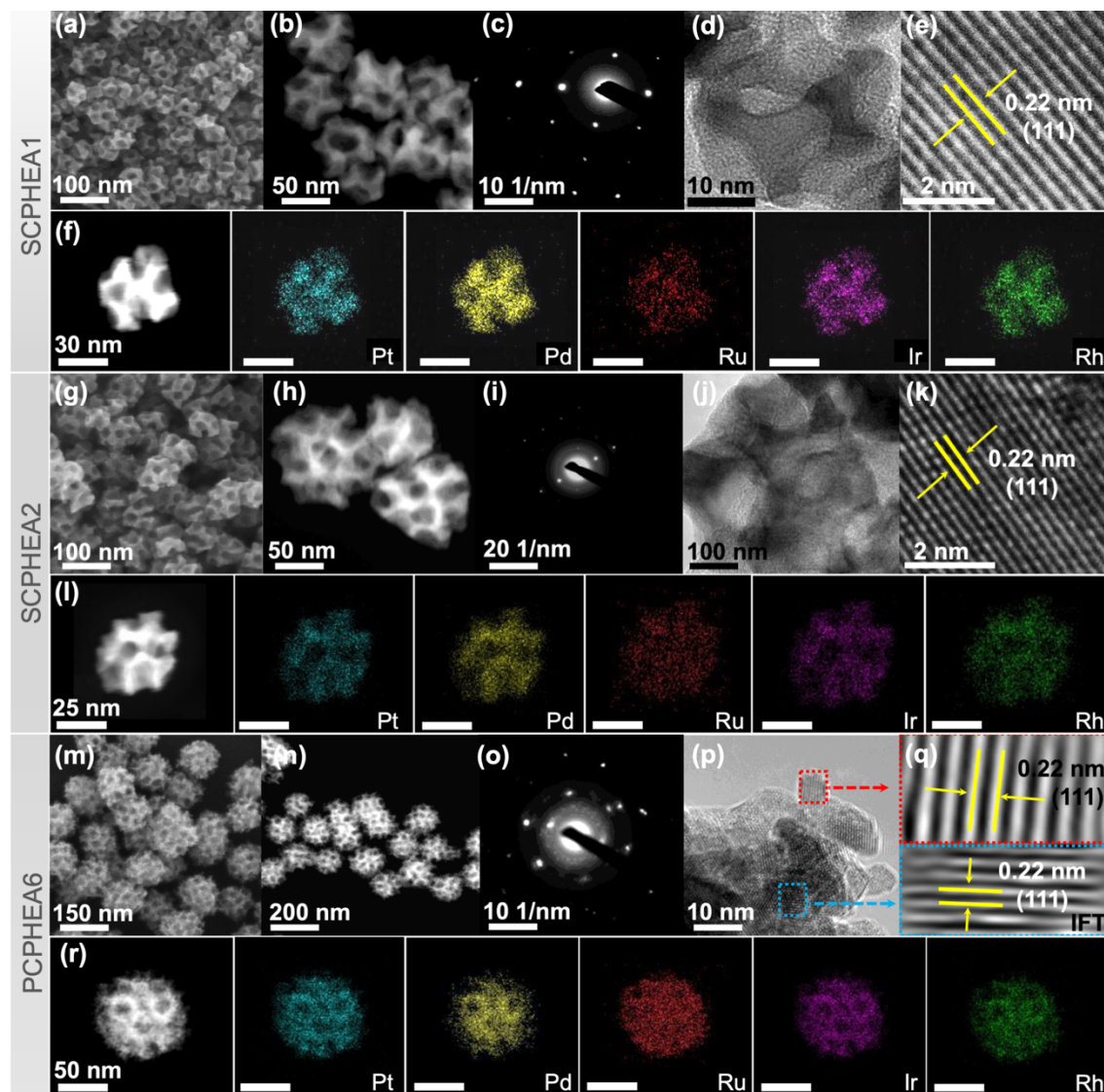


Figure 3. Time-dependent electron microscopic analyses. The representative SEM (a, g, m), HAADF-STEM (b, h, n) images, SAED pattern (c, i, o), TEM image (d, j, p), and concomitant crystal planes (e, k, q) for SCPHEA1, SCPHEA2, PCPHEA6 nanostructure, respectively. (f, l, r) HAADF-STEM images of SCPHEA1, SCPHEA2, and PCPHEA6

were subjected to EDS mapping and corresponding elemental distribution patterns of Pt, Pd, Ru Ir, and Rh, respectively.

Following the observed growth trend, the overall size of the mesoporous HEA particles further increases to 100 ± 10 nm after a 6-hour reaction (PCPHEA6, Figure 3m, n). Notably, while the SAED pattern still exhibits intense bright spots, it now shows a random arrangement too (Figure 3o, Figure S14), indicating a polycrystalline nature, unlike SCPHEA1, 2, and 4. This transition is further supported by HRTEM images of PCHEA6 (Figure 3o, Figure S15), which no longer reveal the seamless, grain-free single structure seen at earlier time points. These results suggest that after 4 hours, growth proceeds via the aggregation of smaller nanoparticles around the larger nanostructure framework, stabilizing surface energy (Figure 3p, q, Figure S15). EDS analysis in HAADF-STEM mode confirms the uniform distribution of Pt/Pd/Ru/Ir/Rh elements (Figure 3r). Overall, the data strongly indicates that reaction time plays a critical role in determining the crystallinity of complex multimetallic nanostructures like HEAs.

Electro-oxidation of Methanol

To evaluate the electrochemical efficacy of single-crystal porous PtPdRuIrRh HEA nanostructures, the methanol electro-oxidation reaction (MOR), an inherently complex process involving $6e^-$ transfer and multiple intermediate species, including CO moiety, was employed as a model reaction (Figure 4).⁵⁵ While Pt-based systems are considered to be the choice of electrocatalysts for MOR, they suffer from CO poisoning, which blocks active sites and severely reduces the overall activity.^{55–59} Here, we performed a comparative study between four different catalysts: the single-crystal porous HEA nanostructure (SCPHEA4), the polycrystalline porous HEA nanostructure (PCPHEA6),

commercially available Pt-C (20 wt. % Pt loading), and a non-porous HEA nanostructure (NPHEA4). The latter was prepared without copolymer micelles under similar experimental conditions used for SCPHEA4, serving as a control to evaluate the effect of porosity.

Prior to the MOR study, the electrochemically active surface area (ECSA) of electrocatalysts was evaluated by employing hydrogen underpotential deposition (HUPD) measurement (Table S2 and Figure S16). It is shown that SCPHEA4 (37.68 m^2/g) and PCPHEA6 (32.72 m^2/g) exhibited superior ECSA compared to NPHEA4 (27.74 m^2/g). The results clearly demonstrate the advantage of our copolymer approach in increasing the effective surface area in complex systems like HEA. A similar trend was observed when impedance spectroscopy (EIS, Figure S17, Table S3) and rate-dependent cyclic voltammetry (CV, Figure S18, Table S4) in non-Faradic regions were employed to estimate the double-layer capacitance (C_{dl}), a quantity directly proportional to ECSA of the catalyst.³¹ During MOR, all electrocatalysts display anodic peaks corresponding to the oxidation of methanol and intermediates (Figure 4a).^{58,60,61} SCPHEA4 demonstrated higher MOR areal specific current density ($\sim 0.61 \text{ mA}/\text{cm}^2$) compared to PCPHEA6 (0.52 mA/cm^2) and NPHEA4 (0.25 mA/cm^2) under similar experimental conditions. The higher J_f/J_b ratio (J_f and J_b are the forward and backward peak current density, respectively) for SCPHEA4 (8.1) compared to PCPHEA6 (3.2) and NPHEA4 (2.5) implies effective electro-oxidation of methanol on SCPHEA4 during the forward potential scan (Figure 4d). SCPHEA4 produces fewer intermediate species and seems to show higher tolerance to poisoning of electroactive sites by intermediates such as CO.^{58–62} SCPHEA4 achieves a mass-specific activity of $\sim 2.7 \text{ A mg}_{\text{Pt}}^{-1}$, which is nearly 1.6 and 4.5 times higher than PCPHEA6 ($\sim 1.6 \text{ A mg}_{\text{Pt}}^{-1}$) and commercial Pt-C ($\sim 0.6 \text{ A mg}_{\text{Pt}}^{-1}$) electrocatalysts,

1 respectively (Figure 4b). Furthermore, the lower onset potential for MOR on SCPHEA4
 2 (~ 0.510 V) compared to Pt-C (~ 0.540 V) and PCPHEA6 (~ 0.545 V, Figure 4c) suggests
 3 higher adsorption and activation ability of SCPHEA4 towards methanol molecules.⁶¹
 4 Noticeably, SCPHEA4 exhibits a lower MOR peak potential ($E_f \sim 0.820$ V at J_f) and a
 5 smaller potential separation between forward and backward anodic peaks ($E_f - E_b \sim 130$
 6 mV) compared to Pt-C ($E_f \sim 1.010$ V and $E_f - E_b \sim 260$ mV) (Figure 4b, d). These
 7 observations indicate that the MOR is kinetically more favorable on SCPHEA4.^{55,57,62–64}
 8 Consequently, SCPHEA4 offers superior MOR mass activity compared to recently
 9 reported precious metal-based HEA and traditional alloy electrocatalysts (Figure 4e,
 10 Table S5). Although higher alkaline concentrations typically enhance methanol oxidation
 11 reaction activity,^{65–67} the single-crystal high-entropy alloy system SCPHEA4 exhibits
 12 comparatively superior MOR performance even in a relatively dilute alkaline solution
 13 (0.1 M KOH electrolyte). This outperforms several previously reported systems operating
 14 in more concentrated alkaline solutions (1.0 M KOH electrolyte, Table S5), indicating the
 15 inherently facile methanol oxidation capability of single-crystal HEA systems.⁶⁵ Figures
 16 4a and 4b further provide valuable insight into the role of mesoporosity and crystallinity
 17 on the enhanced MOR performance of SCPHEA4. The porous SCPHEA4 (~ 0.61
 18 mA/cm²) demonstrates MOR activity nearly 2.5 times larger than that of the nonporous
 19 NPHEA4 (~ 0.25 mA/cm², Figure 4a), which can be attributed to the significantly
 20 improved diffusion coefficient in the porous structure. Randles–Sevcik analysis (Figure
 21 S19) reveals that the diffusion coefficient for porous SCPHEA4 system (5.7×10^{-8} cm²/s)
 22 is an order of magnitude greater than that of NPHEA4 (9.4×10^{-9} cm²/s), underscoring
 23 the critical role of mesoporosity in promoting deeper methanol oxidation.⁶⁸ Furthermore,
 24 among porous systems, single-crystalline SCPHEA4 exhibits superior charge transfer

properties, as indicated by Nyquist plots showing a markedly lower charge transfer resistance throughout the MOR potential window (Figure S20).

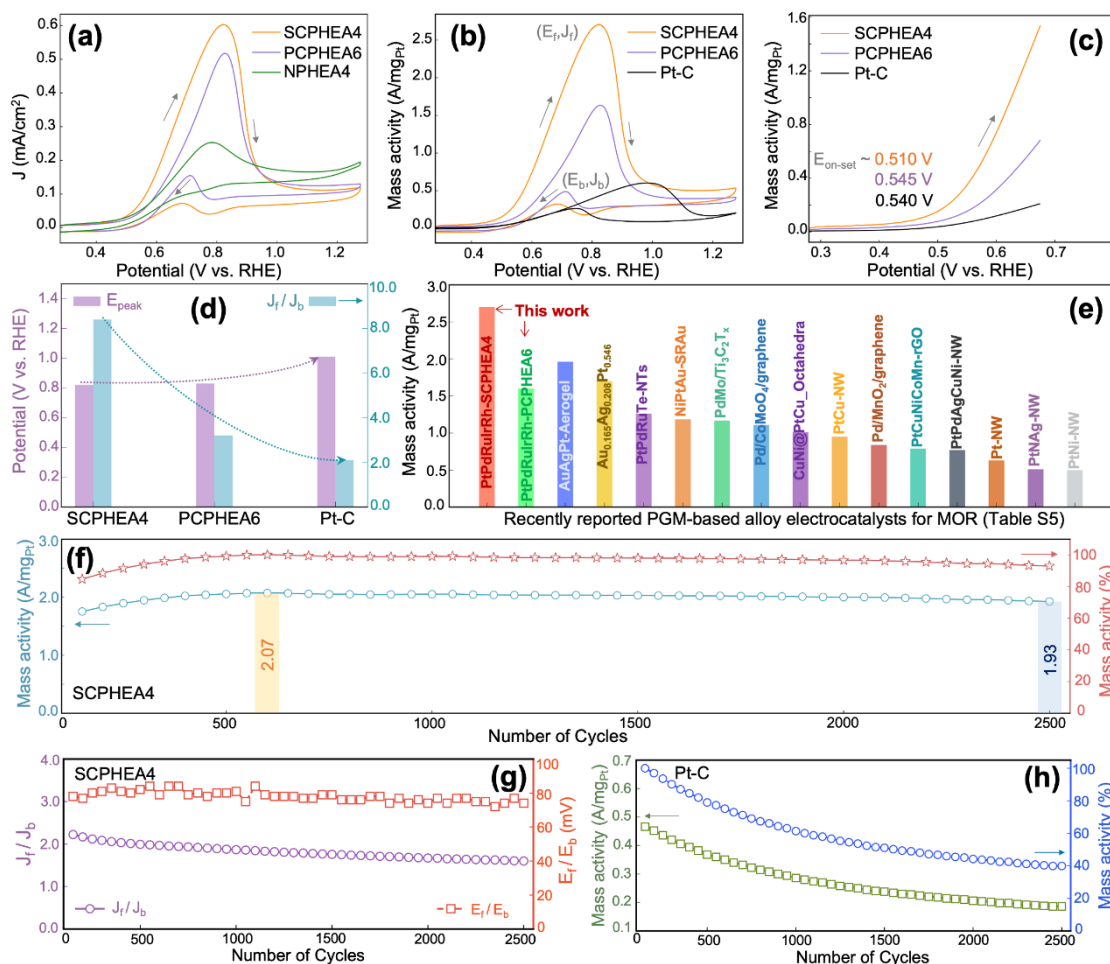


Figure 4. Electrochemical characterization of SCPHEA4. (a) CV curves for NPHEA4, PCPHEA6, and SCPHEA4 were obtained in 0.1 M KOH + 0.5 M methanol aqueous solution. (b) Comparative MOR mass activity of Pt-C, PCPHEA6, and SCPHEA4. (c) CV profiles of forward scan in the potential window of 0.28 to 0.7 V, (d) J_f/J_b , and E_{peak} for Pt-C, PCPHEA6, and SCPHEA4. (e) The mass activity of SCPHEA4 and PCPHEA6 compared to some recently reported multimetallic HEA, and platinum group metals-based electrocatalysts (tabulated in Table S5). (f) Cyclic stability test on SCPHEA4. (g)

Variation profiles of J_f/J_b and $E_f - E_b$, with the number of cycles on SCPHEA4 during the cyclic stability test. h) Cyclic stability test on Pt-C. The inset (Figure f) shows changes in mass activity during cyclic stability. The scan speed used for MOR was 50 mV/s.

To further elucidate the role of mesoporous structure, crystallinity (single crystal vs. polycrystal), and high-entropy alloying features, we also evaluated the long-term operational stability of several samples, including non-porous/NPHEA4, single-crystal/SCPHEA4, polycrystalline/PCPHEA6, and commercial Pt-C electrocatalysts. Among them, SCPHEA4 exhibited exceptional durability, retaining approximately 93% of its maximum MOR current density after 2500 cycles (Figure 4f and Figure S21) while maintaining a stable J_f/J_b ratio and a nearly constant $E_f - E_b$ value (Figure 4g). These results indicate SCPHEA4's inherent ability to sustain efficient methanol electro-oxidation by effectively handling reaction intermediates over extended periods.^{56,59,60,63} This outstanding performance is attributed to a combination of entropy-stabilized, robust structural features (Figure 5a–c), the presence of a wide range of active sites in the HEA system (Figure 2o and Figure 6), and the efficient charge transfer enabled by its single-crystalline nature (Figure S20). In contrast, the commercial Pt-C electrocatalyst suffered a rapid decline in MOR activity, losing approximately 60% of its maximum current density under identical reaction conditions (Figure 4h and Figure S21). This degradation is primarily due to intermediate-induced blocking of active sites and structural instability under aggressive operating conditions (Figure 5d–f).^{55,59} Similarly, the non-porous NPHEA4 and polycrystalline PCPHEA6 also experienced significant performance losses, with ~31% and ~70% reductions in current density, respectively (Figure S21) post 2500 cycles elucidating the role of single crystal systems for sustained MOR performance.

These findings collectively demonstrate that achieving both high activity and long-term stability in methanol oxidation requires the synergistic integration of single crystallinity, mesoporous structure, and high-entropy alloy composition.

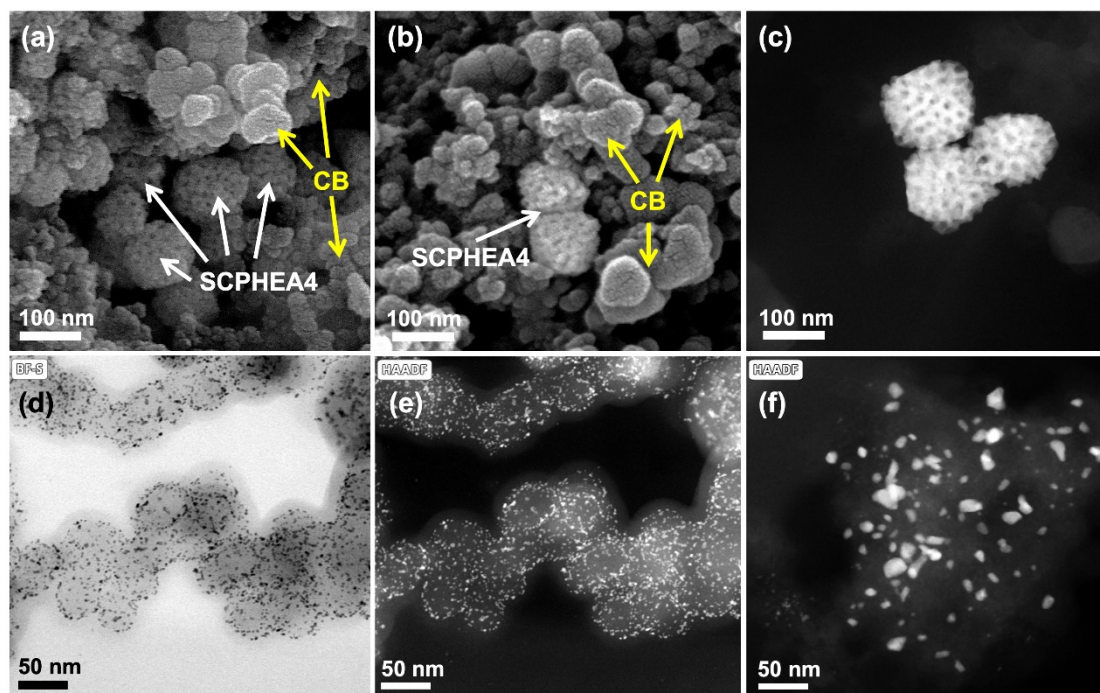


Figure 5. Electron microscopic observations. (a,b) SEM and (c) HAADF-STEM images of SCPHEA4 post-MOR cyclic studies. TEM images of commercial Pt-C electrocatalyst (d,e) fresh and (f) post-MOR cyclic studies. (CB- Carbon Black nanoparticles were used during catalytic ink preparation).

Chronoamperometric studies conducted at 0.675 V further demonstrate that SCPHEA4 exhibits a lower current decay compared to both PCPHEA6 and NPHEA4 (Figure S22), indicating greater tolerance toward and more efficient management of the reaction intermediates generated during MOR.⁶¹ This observation is consistent with the CV results presented in Figures 4a, 4f, and S21. Collectively, the CA studies support that SCPHEA4

nanostructures comparatively offer both enhanced and stable performance for MOR. In conclusion, the MOR electrochemical screening indicates that our single-crystal porous PtPdRuIrRh HEA nanostructures provide high areal and mass-specific activities, effective overall electro-oxidation, and excellent current retention ability. All these advantages are likely related to their ability to suppress poisoning caused by reaction intermediates.

Computational Insights

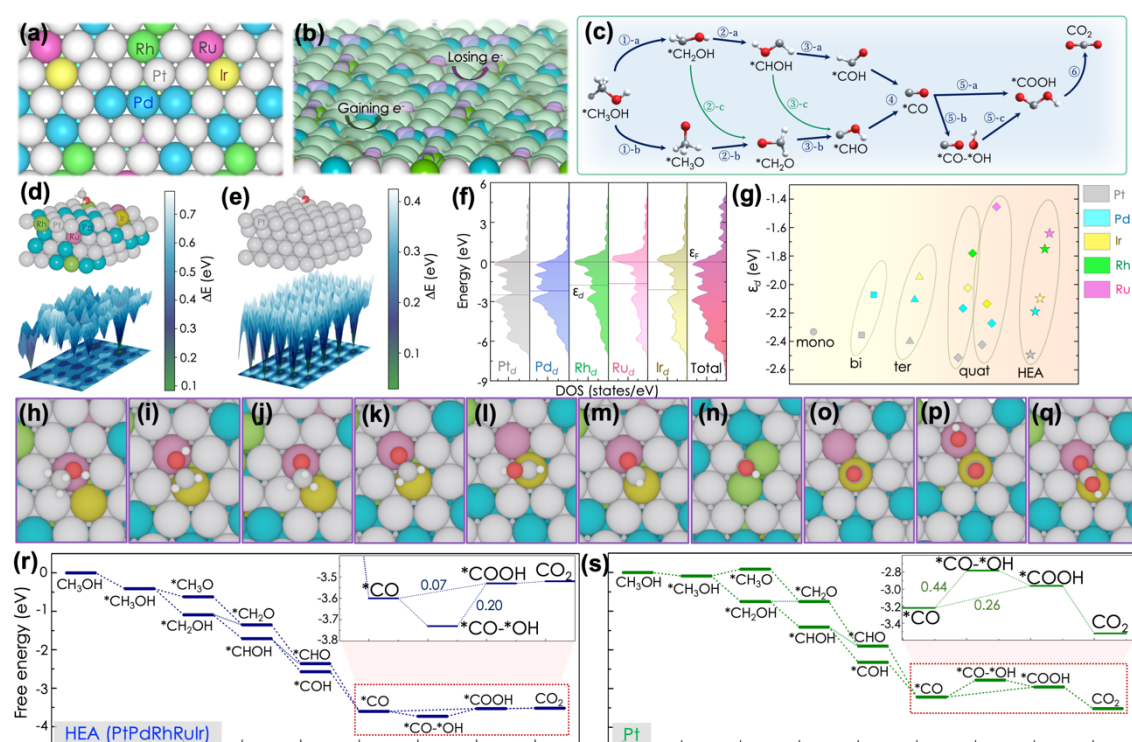


Figure 6. Computational insights of MOR process on PtPdRuIrRh HEA systems. Top views of (a) optimized HEA surface (where the grey, cyan, green, yellow, and magenta balls represent Pt, Pd, Rh, Ir, and Ru atoms, respectively) and (b) charge density distribution on the HEA surface (green: gaining electron region, purple: losing electron region). (c) The MOR mechanism on metal surfaces with different intermediates, where

* indicates adsorbed species. The energy landscape perspective of CH₃OH molecule on (d) PtPdRhIrRu HEA and (e) Pt. (f) The total DOS and partial DOSs of Pt-5*d*, Pd-4*d*, Rh-4*d*, Ru-4*d*, and Ir-5*d* orbitals in HEA. The Fermi level ε_F is referred to at 0 eV, and ε_d is the *d*-band center position. (g) The change of the *d*-band center of elements in mono, binary (PtPd), ternary (PtPdIr), quaternary (PtPdIrRh), and HEA (PtPdIrRhRu) alloys. (h-q) Stable adsorption configurations of intermediates for optimal MOR pathways on HEA surface from a top view including (h) *CH₃OH, (i) *CH₂OH, (j) *CH₃O, (k) *CH₂O, (l) *CHOH, (m) *CHO, (n) *COH, (o) *CO, (p) *CO-*OH, (q) *COOH. (r,s) Free-energy diagrams of optimal reaction pathways for the MOR at 0.6 V versus RHE on HEA and Pt catalysts.

To understand the mechanism and explain the enhancement of MOR performance on SCPHEA, density functional theory (DFT) calculations were performed on the (111) facet of HEA PtPdIrRhRu compared with five Pt-based catalysts including Pt, binary PtPd, ternary PtPdIr, quaternary PtPdIrRh, and quaternary PtPdIrRu alloys (Figure 6 and Figure S23). The DFT calculations reveal that the HEA surface, alongside other surfaces, is pretty stable regarding its structural integrity, which is mainly attributed to the Pt richness (Figure 6a, b, and Figure S23). Regarding electronic structure, the differences in the electronegativity of the elements led to a redistribution of charges on the surfaces (Figure 6a and b). Particularly, valence electrons of non-Pt-atoms tend to be transferred to neighboring Pt atoms due to the higher electronegativity (2.98) as compared to Ir (2.79), Pd (2.70), Ru (2.68), and Rh (2.65).⁵¹ This charge transfer results in the formation of electron-deficient regions (Figure 6b) around non-Pt atoms (see also Table S6 for the Bader charge analysis). As a result, this depletion of electrons may influence how the surface interacts with methanol and MOR reaction intermediates. For instance, CH₃OH

tends to bind to non-Pt centers (particularly on Ru, Rh, or Ir), as illustrated in the potential energy landscape for CH₃OH adsorption on HEA (Figure 6d).⁵⁵ The adsorption energies of CH₃OH on these sites are 0.2–0.3 eV more stable than on the pure Pt surface (Figure 6e). This observation agrees with the experimental findings where the SCPHEA4 exhibited a comparatively lower onset potential (Figure 4c), indicating stronger methanol adsorption and activation ability towards MOR.⁶¹ This tendency is also observed in the cases of binary, ternary, and quaternary alloys (Figure S24). It appears that with an increase in alloying metals, more favorable active sites emerge. The detailed electronic structure, shown by the partial density of states (DOS) of HEA, further supports this finding (Figure 6f,g). In particular, the *d*-band centers of Ru, Rh, Ir, or Pd atoms were closer to the Fermi level than that of Pt atoms. The higher *d*-states of these atoms may disclose more empty antibonding states at the Fermi level, leading to stronger binding to adsorbates than Pt sites. In conclusion, based on CH₃OH adsorption, we can rank the efficiency of surfaces as PtPdIrRhRu (HEA) > PtPdIrRu > PtPdIrRh > PtPdIr > PtPd > Pt.

The MOR mechanism on the HEA surface was compared with other Pt-based alloys to explain HEA's superior catalytic activity (Figures S24, S25). The most stable adsorption configurations of eight key reaction intermediates on HEA are depicted in Figure 6h-q, where different intermediates favor different active sites. For example, CH₃OH and CH₃O adsorb at Ru top sites, whereas CH₂OH, CH₂O, CHO, and COOH prefer to bridge between Ru-Ir sites. This diversity of active sites could ensure the superior MOR performance of the HEA surface compared to other Pt-alloyed surfaces. In Figure 6r, s, and Figure S25, we present the free-energy diagrams for optimal MOR pathways of the six Pt-based catalysts, calculated at an electrode potential of 0.6 V versus RHE (see also

Table S6- S14). The reaction pathways are generally downhill in energy. Here, we looked closely into CO poisoning since it is believed to affect the overall MOR performance significantly.^{55,56,58,59} To overcome CO poisoning, two strategies could be employed: (i) weakening CO adsorption and (ii) enhancing water dissociation to produce hydroxyl species that oxidize CO to CO₂.⁵⁶ We observed that the Pt monometallic system is relatively inefficient at dissociating water. The water dissociation free energy (on a CO-poisoned Pt surface) $*CO + H_2O \rightarrow *CO-*OH + (H^+ + e^-)$ is endergonic by 0.44 eV. This explains why the Pt monometallic system is highly susceptible to CO poisoning, as reflected in the experimental Pt-C MOR study (Figure 4b-f,h). On the other hand, alloying Pt with other metals could enhance water dissociation, with the reaction becoming less endergonic from binary PtPd to ternary PtPdIr and quaternary PtPdIrRh alloys. Notably, we found that the reaction free energy on PtPdIrRu becomes negative (i.e., exergonic) while reaching the most negative value (i.e., -0.13 eV) on PtPdIrRhRu. This suggests that the MOR activities on the HEA and quaternary PtPdIrRu alloys should be competitive but surpass those of the remaining Pt-based alloys. The excellent ability of HEA to dissociate water is expected to increase *OH production, thereby promoting the CO depoisoning process. This was experimentally observed on SCPHEA4: (i) the J_f/J_b ratio was higher than the other electrocatalysts (Figure 4a,b,d), and (ii) this ratio remained stable during the cyclic study (Figure 4 f-h).

CONCLUSIONS

In summary, this study demonstrates the block copolymer micelle-assisted synthesis of mesoporous single-crystal high-entropy alloys (HEAs) composed of PtPdRuIrRh via an

all-wet-chemical reduction approach. The systematic investigation underscores the crucial roles of block polymers, chemical conditions, temperature, and reaction time in controlling the crystallinity and morphology of the HEA nanostructures. The optimized single-crystal mesoporous HEA features uniformly sized mesopores that permeate the entire structure, ensuring exposure to high-entropy electroactive sites and enhancing charge and mass transport. For MOR catalysis, the optimized single-crystal mesoporous HEA exhibits superior catalytic activity, with the lowest onset and peak potentials, compared to polycrystalline counterparts, commercial Pt-C electrocatalysts, recently reported precious metal-based HEAs, and traditional alloys. Combining experimental observations with computational calculations, the study reveals that mesoporous single-crystal HEA systems effectively mitigate CO poisoning during MOR by enhancing water dissociation, resulting in extended cyclic stability. Overall, this work provides a soft-chemical design strategy for creating multimetallic porous single-crystal HEA systems with mesoporous architectures, applicable to fundamental research and applications beyond electrocatalysis.

ASSOCIATED CONTENT

Supporting Information

UV-visible absorbance spectra of metal salt solutions with and without copolymer micelles, an optical image of Tyndall's effect, and additional SAED patterns and EDS-TEM elemental line scan data, mappings, distribution profiles, and ICP-OES. SEM images of HEA nanostructures for temperature, copolymers, precursor chemicals variation, and electrochemical data (HUPD/EIS/CV) for ECSA determination, additional electrochemical data, along with a MOR comparison table. Experimental methods for

synthesizing various HEA nanostructures, the methodology used, and computational data.

The Supporting Information is available free of charge.

AUTHOR INFORMATION

Corresponding Author

Joel Henzie – Research Center for Materials Nanoarchitectonics, National Institute for Materials Science (NIMS), 1-1 Namiki, Tsukuba, Ibaraki 305-0044, Japan.

Email: HENZIE.Joeladam@nims.go.jp, orcid.org/0000-0002-9190-2645

Ho Ngoc Nam - Department of Materials Process Engineering, Graduate School of Engineering, Nagoya University, Furo-cho, Chikusa-ku, Nagoya 464-8603, Japan.

Email: honam@nagoya-u.jp, orcid.org/0000-0001-9785-5061.

Yusuke Yamauchi – School of Chemical Engineering and Australian Institute for Bioengineering and Nanotechnology (AIBN), The University of Queensland, Brisbane, Queensland 4072, Australia.

Department of Materials Process Engineering, Graduate School of Engineering, Nagoya University, Nagoya 464-8603, Japan.

Email: y.yamauchi@uq.edu.au, orcid.org/0000-0001-7854-927X.

Authors

Ravi Nandan –Research Center for Materials Nanoarchitectonics, National Institute for Materials Science (NIMS), 1-1 Namiki, Tsukuba, Ibaraki 305-0044, Japan.

orcid.org/0000-0001-9244-3594.

Quan Manh Phung - Department of Chemistry, Graduate School of Science, Nagoya University, Furo-cho, Chikusa-ku, Nagoya 464-8602, Japan.

Institute of Transformative Bio-Molecules (WPI-ITbM), Nagoya University, Furo-cho, Chikusa-ku, Nagoya 464-8601, Japan.

orcid.org/0000-0001-8205-5328.

Hiroki Nara - Waseda Research Institute for Science and Engineering, Waseda University, 3-4-1 Okubo, Shinjuku Tokyo 169-8555, Japan.

orcid.org/0000-0002-1356-9429.

Author Contributions

R.N.: Conceptualization and methodology, HEA materials synthesis, data analysis, original draft writing, editing, and review of the manuscript. H.N.N. and Q.M.P.: Computational studies and concomitant data analysis, scientific discussions, writing and editing manuscript. H.N.: Electrochemical data analysis, discussion, review, and editing of the manuscript. J.H.: Conceptualization, TEM measurements and data curation, scientific discussions, supervision, manuscript review, and editing. Y.Y.: Conceptualization, scientific discussions, funding acquisition, overall supervision, project administration, review, and manuscript editing.

The manuscript was written through the contributions of all authors. All authors have approved the final version of the manuscript.

Funding Sources

The authors are thankful to the Japan Society for the Promotion of Science (JSPS No. P22063), Japan Science and Technology Corporation (JPMJER2003), and JSPS Grants-

in-Aid for Scientific Research KAKENHI Program (20K05453, 24K17694) for funding support.

Notes

There are no conflicts to declare.

ACKNOWLEDGMENT

The authors would like to acknowledge the support from the JST-ERATO Yamauchi Materials Space-Tectonics Project (JPMJER2003). R.N. and Y.Y. acknowledge financial support from the Japan Society for the Promotion of Science (JSPS, No. P220632). J.H. acknowledges financial support from the JSPS Grants-in-Aid for Scientific Research KAKENHI Program (20K05453). H.N.N thanks the supercomputer systems at the Institute for Solid State Physics, The University of Tokyo, for providing computational facilities. Q.M.P acknowledges financial support from JSPS KAKENHI (24K17694) and Research Center for Computational Science, Okazaki, for computational resources (Projects: 24-IMS-C082 and 23-IMS-C087).The authors express the gratitude for the English editing software, such as Grammarly and ChatGPT, for the language refining and checking grammatical errors in the manuscript.

REFERENCES

- (1) Lv, H.; Wang, Y.; Sun, L.; Yamauchi, Y.; Liu, B. A General Protocol for Precise Syntheses of Ordered Mesoporous Intermetallic Nanoparticles. *Nature Protocols* 2023 18:10 **2023**, 18 (10), 3126–3154. <https://doi.org/10.1038/s41596-023-00872-1>.
- (2) Yin, S.; Liu, L.; Li, J.; Wu, H.; Lv, Z.; He, Y.; Zhang, J. Y.; Zhang, P.; Zhao, Z.;

- 1 Zhao, D.; Lan, K. Mesoporous TiO₂ Single-Crystal Particles from Controlled
2 Crystallization-Driven Mono-Micelle Assembly as an Efficient Photocatalyst. *J*
3 *Am Chem Soc* **2024**, *146* (2), 1701–1709. <https://doi.org/10.1021/JACS.3C12727>.
- 4 (3) Wu, T.; Chen, G.; Han, J.; Sun, R.; Zhao, B.; Zhong, G.; Yamauchi, Y.; Guan, B.
5 Construction of Three-Dimensional Dendritic Hierarchically Porous Metal-
6 Organic Framework Nanoarchitectures via Noncentrosymmetric Pore-Induced
7 Anisotropic Assembly. *J Am Chem Soc* **2023**, *145* (30), 16498–16507.
8 <https://doi.org/10.1021/JACS.3C03029>.
- 9 (4) Lv, H.; Mao, Y.; Yao, H.; Ma, H.; Han, C.; Yang, Y. Y.; Qiao, Z. A.; Liu, B. Ir-
10 Doped CuPd Single-Crystalline Mesoporous Nanotetrahedrons for Ethylene
11 Glycol Oxidation Electrocatalysis: Enhanced Selective Cleavage of C–C Bond.
12 *Angewandte Chemie International Edition* **2024**, *63* (15), e202400281.
13 <https://doi.org/10.1002/ANIE.202400281>.
- 14 (5) Song, Y.; Song, X.; Wang, X.; Bai, J.; Cheng, F.; Lin, C.; Wang, X.; Zhang, H.;
15 Sun, J.; Zhao, T.; Nara, H.; Sugahara, Y.; Li, X.; Yamauchi, Y. Two-Dimensional
16 Metal-Organic Framework Superstructures from Ice-Templated Self-Assembly. *J*
17 *Am Chem Soc* **2022**, *144* (38), 17457–17467.
18 <https://doi.org/10.1021/JACS.2C06109>.
- 19 (6) Kang, Y.; Masud, M. K.; Guo, Y.; Zhao, Y.; Nishat, Z. S.; Zhao, J.; Jiang, B.;
20 Sugahara, Y.; Pejovic, T.; Morgan, T.; Hossain, M. S. A.; Li, H.; Salomon, C.; Asahi,
21 T.; Yamauchi, Y. Au-Loaded Superparamagnetic Mesoporous Bimetallic CoFeB
22 Nanovehicles for Sensitive Autoantibody Detection. *ACS Nano* **2023**, *17* (4),
23 3346–3357. <https://doi.org/10.1021/ACSNANO.2C07694>.
- 24 (7) Lv, H.; Liu, B. Two-Dimensional Mesoporous Metals: A New Era for Designing

- Functional Electrocatalysts. *Chem Sci* **2023**, *14* (46), 13313–13324.
<https://doi.org/10.1039/D3SC04244H>.
- (8) Li, J.; Xia, W.; Xu, X.; Jiang, D.; Cai, Z. X.; Tang, J.; Guo, Y.; Huang, X.; Wang, T.; He, J.; Han, B.; Yamauchi, Y. Selective Etching of Metal-Organic Frameworks for Open Porous Structures: Mass-Efficient Catalysts with Enhanced Oxygen Reduction Reaction for Fuel Cells. *J Am Chem Soc* **2023**, *145* (50), 27262–27272.
<https://doi.org/10.1021/JACS.3C05544>.
- (9) Yang, C.; Gao, Y.; Ma, T.; Bai, M.; He, C.; Ren, X.; Luo, X.; Wu, C.; Li, S.; Cheng, C. Metal Alloys-Structured Electrocatalysts: Metal–Metal Interactions, Coordination Microenvironments, and Structural Property–Reactivity Relationships. *Advanced Materials* **2023**, *35* (51), 2301836.
<https://doi.org/10.1002/ADMA.202301836>.
- (10) Furukawa, S.; Komatsu, T.; Shimizu, K. I. Catalyst Design Concept Based on a Variety of Alloy Materials: A Personal Account and Relevant Studies. *J Mater Chem A Mater* **2020**, *8* (31), 15620–15645. <https://doi.org/10.1039/D0TA03733H>.
- (11) Qing-Miao, H.; Rui, Y. The Endless Search for Better Alloys. *Science (1979)* **2022**, *378* (6615), 26–27. <https://doi.org/10.1126/SCIENCE.ADE5503>.
- (12) Poncet, V.; Bond, G. C. Geoffrey C. Catalysis by Metals and Alloys. **1995**, 734.
- (13) Jiang, B.; Li, C.; Imura, M.; Tang, J.; Yamauchi, Y. Multimetallic Mesoporous Spheres Through Surfactant - Directed Synthesis. *Advanced Science* **2015**, *2* (8).
<https://doi.org/10.1002/ADVS.201500112>.
- (14) Iqbal, M.; Kim, Y.; Li, C.; Jiang, B.; Takei, T.; Lin, J.; Yuliarto, B.; Bando, Y.; Henzie, J.; Yamauchi, Y. Tailored Design of Mesoporous PdCu Nanospheres with Different Compositions Using Polymeric Micelles. *ACS Appl Mater Interfaces*

1 **2019**, *11* (40), 36544–36552. <https://doi.org/10.1021/ACSAMI.9B09737>.

2 (15) Rodrigues, T. S.; da Silva, A. G. M.; Macedo, A.; Farini, B. W.; Alves, R. da S.;
3 Camargo, P. H. C. Probing the Catalytic Activity of Bimetallic versus Trimetallic
4 Nanoshells. *J Mater Sci* **2015**, *50* (16), 5620–5629.
5 <https://doi.org/10.1007/S10853-015-9114-X/METRICS>.

6 (16) Dey, G. R.; McCormick, C. R.; Soliman, S. S.; Darling, A. J.; Schaak, R. E.
7 Chemical Insights into the Formation of Colloidal High Entropy Alloy
8 Nanoparticles. *ACS Nano* **2023**, *17* (6), 5943–5955.
9 <https://doi.org/10.1021/ACSNANO.3C00176>.

10 (17) Yao, Y.; Dong, Q.; Brozena, A.; Luo, J.; Miao, J.; Chi, M.; Wang, C.; Kevrekidis,
11 I. G.; Ren, Z. J.; Greeley, J.; Wang, G.; Anapolsky, A.; Hu, L. High-Entropy
12 Nanoparticles: Synthesis-Structureproperty Relationships and Data-Driven
13 Discovery. *Science (1979)* **2022**, *376* (6589).
14 <https://doi.org/10.1126/SCIENCE.ABN3103>.

15 (18) Dragoe, N.; Bérardan, D. Order Emerging from Disorder. *Science (1979)* **2019**,
16 *366* (6465), 573–574. <https://doi.org/10.1126/SCIENCE.AAZ1598>.

17 (19) Sun, Y.; Dai, S. High-Entropy Materials for Catalysis: A New Frontier. *Sci Adv*
18 **2021**, *7* (20). <https://doi.org/10.1126/SCIADV.ABG1600>.

19 (20) Huang, Z.; Li, T.; Li, B.; Dong, Q.; Smith, J.; Li, S.; Xu, L.; Wang, G.; Chi, M.;
20 Hu, L. Tailoring Local Chemical Ordering via Elemental Tuning in High-Entropy
21 Alloys. *J Am Chem Soc* **2024**, *146* (3), 2167–2173.
22 <https://doi.org/10.1021/JACS.3C12048>.

23 (21) Xu, W.; Diesen, E.; He, T.; Reuter, K.; Margraf, J. T. Discovering High Entropy
24 Alloy Electrocatalysts in Vast Composition Spaces with Multiobjective

- Optimization. *J Am Chem Soc* **2023**. <https://doi.org/10.1021/JACS.3C14486>.
- (22) Nandan, R.; Raj, G.; Nanda, K. K. FeCoNiMnCr High-Entropy Alloy Nanoparticle-Grafted NCNTs with Promising Performance in the Ohmic Polarization Region of Fuel Cells. *ACS Appl Mater Interfaces* **2022**, *14* (14), 16108–16116. <https://doi.org/10.1021/ACSAMI.1C21336>.
- (23) Broge, N. L. N.; Bondesgaard, M.; Søndergaard-Pedersen, F.; Roelsgaard, M.; Iversen, B. B. Autocatalytic Formation of High-Entropy Alloy Nanoparticles. *Angewandte Chemie* **2020**, *132* (49), 22104–22108. <https://doi.org/10.1002/ANGE.202009002>.
- (24) Tao, L.; Sun, M.; Zhou, Y.; Luo, M.; Lv, F.; Li, M.; Zhang, Q.; Gu, L.; Huang, B.; Guo, S. A General Synthetic Method for High-Entropy Alloy Subnanometer Ribbons. *J Am Chem Soc* **2022**, *144* (23), 10582–10590. <https://doi.org/10.1021/JACS.2C03544>.
- (25) Raj, G.; Nandan, R.; Kumar, K.; Gorle, D. B.; Mallya, A. B.; Osman, S. M.; Na, J.; Yamauchi, Y.; Nanda, K. K. High Entropy Alloying Strategy for Accomplishing Quintuple-Nanoparticles Grafted Carbon towards Exceptional High-Performance Overall Seawater Splitting. *Mater Horiz* **2023**, *10* (11), 5032–5044. <https://doi.org/10.1039/D3MH00453H>.
- (26) Mao, Q.; Mu, X.; Deng, K.; Yu, H.; Wang, Z.; Xu, Y.; Li, X.; Wang, L.; Wang, H. Multisite Synergism-Induced Electron Regulation of High-Entropy Alloy Metallene for Boosting Alkaline Hydrogen Evolution Reaction. *Adv Funct Mater* **2023**, *33* (42), 2304963. <https://doi.org/10.1002/ADFM.202304963>.
- (27) Batchelor, T. A. A.; Pedersen, J. K.; Winther, S. H.; Castelli, I. E.; Jacobsen, K. W.; Rossmeisl, J. High-Entropy Alloys as a Discovery Platform for Electrocatalysis.

- Joule* **2019**, 3 (3), 834–845. <https://doi.org/10.1016/J.JOULE.2018.12.015>.
- (28) Wang, B.; Yao, Y.; Yu, X.; Wang, C.; Wu, C.; Zou, Z. Understanding the Enhanced Catalytic Activity of High Entropy Alloys: From Theory to Experiment. *J Mater Chem A Mater* **2021**, 9 (35), 19410–19438. <https://doi.org/10.1039/D1TA02718B>.
- (29) Amiri, A.; Shahbazian-Yassar, R. Recent Progress of High-Entropy Materials for Energy Storage and Conversion. *J Mater Chem A Mater* **2021**, 9 (2), 782–823. <https://doi.org/10.1039/D0TA09578H>.
- (30) Glasscott, M. W. Classifying and Benchmarking High-Entropy Alloys and Associated Materials for Electrocatalysis: A Brief Review of Best Practices. *Curr Opin Electrochem* **2022**, 34, 100976. <https://doi.org/10.1016/J.COEELEC.2022.100976>.
- (31) Nandan, R.; Nara, H.; Nam, H. N.; Phung, Q. M.; Ngo, Q. P.; Na, J.; Henzie, J.; Yamauchi, Y. Tailored Design of Mesoporous Nanospheres with High Entropic Alloy Sites for Efficient Redox Electrocatalysis. *Advanced Science* **2024**, 11 (35), 2402518. <https://doi.org/10.1002/ADVS.202402518>.
- (32) Tang, Y.; Ouyang, M. Tailoring Properties and Functionalities of Metal Nanoparticles through Crystallinity Engineering. *Nature Materials* **2007**, 6 (10), 754–759. <https://doi.org/10.1038/nmat1982>.
- (33) Badwal, S. P. S. Electrical Conductivity of Single Crystal and Polycrystalline Yttria-Stabilized Zirconia. *J Mater Sci* **1984**, 19 (6), 1767–1776. <https://doi.org/10.1007/BF00550246/METRICS>.
- (34) Sanders, M. B.; Krizan, J. W.; Plumb, K. W.; McQueen, T. M.; Cava, R. J. NaSrMn₂F₇, NaCaFe₂F₇, and NaSrFe₂F₇: Novel Single Crystal Pyrochlore Antiferromagnets. *Journal of Physics: Condensed Matter* **2016**, 29 (4), 045801.

1 <https://doi.org/10.1088/1361-648X/29/4/045801>.

2 (35) Browall, K. W.; Kasper, J. S. The Electrical Conductivity of Single Crystals of
3 Ag₂HgI₄. *J Solid State Chem* **1975**, *15* (1), 54–60. [https://doi.org/10.1016/0022-](https://doi.org/10.1016/0022-4596(75)90270-4)
4 4596(75)90270-4.

5 (36) Ahmad, S. I.; Hamoudi, H.; Ponraj, J.; Youssef, K. M. In-Situ Growth of Single-
6 Crystal Plasmonic Aluminum–Lithium-Graphene Nanosheets with a Hexagonal
7 Platelet-like Morphology Using Ball-Milling. *Carbon N Y* **2021**, *178*, 657–665.
8 <https://doi.org/10.1016/J.CARBON.2021.03.053>.

9 (37) Huang, J. S.; Callegari, V.; Geisler, P.; Brüning, C.; Kern, J.; Prangma, J. C.; Wu,
10 X.; Feichtner, T.; Ziegler, J.; Weinmann, P.; Kamp, M.; Forchel, A.; Biagioni, P.;
11 Sennhauser, U.; Hecht, B. Atomically Flat Single-Crystalline Gold Nanostructures
12 for Plasmonic Nanocircuitry. *Nature Communications 2010 1:1* **2010**, *1* (1), 1–8.
13 <https://doi.org/10.1038/ncomms1143>.

14 (38) Kumar, R.; Srivastava, P.; Kumar, T.; Bag, M. Electronic-Ionic Transport in
15 MAPbBr₃ Single Crystal: The Evidence of Super-Linear Power Law in AC
16 Conductivity. *Journal of Physical Chemistry C* **2022**, *126* (33), 14305–14311.
17 <https://doi.org/10.1021/ACS.JPCC.2C04135>.

18 (39) Sharma, A.; Amodeo, J.; Gazit, N.; Qi, Y.; Thomas, O.; Rabkin, E. When More Is
19 Less: Plastic Weakening of Single Crystalline Ag Nanoparticles by the
20 Polycrystalline Au Shell. *ACS Nano* **2021**, *15* (9), 14061–14070.
21 <https://doi.org/10.1021/ACSNANO.1C02976>.

22 (40) Guo, Z. Y.; Sun, R.; Huang, Z.; Han, X.; Wang, H.; Chen, C.; Liu, Y. Q.; Zheng,
23 X.; Zhang, W.; Hong, X.; Li, W. W. Crystallinity Engineering for Overcoming the
24 Activity–Stability Tradeoff of Spinel Oxide in Fenton-like Catalysis. *Proc Natl*

Acad Sci U S A **2023**, *120* (15), e2220608120.

<https://doi.org/10.1073/PNAS.2220608120>.

(41) Mahmoud, M. A.; Tabor, C. E.; El-Sayed, M. A.; Ding, Y.; Zhong, L. W. A New Catalytically Active Colloidal Platinum Nanocatalyst: The Multiarmed Nanostar Single Crystal. *J Am Chem Soc* **2008**, *130* (14), 4590–4591. <https://doi.org/10.1021/JA710646T>.

(42) Kang, Y.; Cretu, O.; Kikkawa, J.; Kimoto, K.; Nara, H.; Nugraha, A. S.; Kawamoto, H.; Eguchi, M.; Liao, T.; Sun, Z.; Asahi, T.; Yamauchi, Y. Mesoporous Multimetallic Nanospheres with Exposed Highly Entropic Alloy Sites. *Nature Communications* **2023**, *14* (1), 1–12. <https://doi.org/10.1038/s41467-023-39157-2>.

(43) Jiang, B.; Xue, H.; Wang, P.; Du, H.; Kang, Y.; Zhao, J.; Wang, S.; Zhou, W.; Bian, Z.; Li, H.; Henzie, J.; Yamauchi, Y. Noble-Metal-Metalloid Alloy Architectures: Mesoporous Amorphous Iridium-Tellurium Alloy for Electrochemical N₂ Reduction. *J Am Chem Soc* **2023**, *145* (11), 6079–6086. <https://doi.org/10.1021/JACS.2C10637>.

(44) Iqbal, M.; Li, C.; Wood, K.; Jiang, B.; Takei, T.; Dag, Ö.; Baba, D.; Nugraha, A. S.; Asahi, T.; Whitten, A. E.; Hossain, M. S. A.; Malgras, V.; Yamauchi, Y. Continuous Mesoporous Pd Films by Electrochemical Deposition in Nonionic Micellar Solution. *Chemistry of Materials* **2017**, *29* (15), 6405–6413. <https://doi.org/10.1021/ACS.CHEMMATER.7B01811>.

(45) Albayrak, C.; Soylu, A. M.; Dag, Ö. Lyotropic Liquid-Crystalline Mesophases of [Zn(H₂O)₆](NO₃)₂-C₁₂EO₁₀-CTAB- H₂O and [Zn(H₂O)₆](NO₃)₂-C₁₂EO₁₀-SDS-H₂O Systems. *Langmuir* **2008**, *24* (19), 10592–10595.

1 <https://doi.org/10.1021/LA8022453>.

2 (46) Boily, J. F.; Seward, T. M. Palladium(II) Chloride Complexation:
3 Spectrophotometric Investigation in Aqueous Solutions from 5 to 125°C and
4 Theoretical Insight into Pd-Cl and Pd-OH₂ Interactions. *Geochim Cosmochim*
5 *Acta* **2005**, 69 (15), 3773–3789. <https://doi.org/10.1016/J.GCA.2005.03.015>.

6 (47) Egerton, R. F. Physical Principles of Electron Microscopy: An Introduction to
7 TEM, SEM, and AEM, Second Edition. *Physical Principles of Electron*
8 *Microscopy: An Introduction to TEM, SEM, and AEM, Second Edition* **2016**, 1–
9 196. <https://doi.org/10.1007/978-3-319-39877-8>.

10 (48) Yan, X. H.; Liaw, P. K.; Zhang, Y. Order and Disorder in Amorphous and High-
11 Entropy Materials. *Metall Mater Trans A Phys Metall Mater Sci* **2021**, 52 (6),
12 2111–2122. <https://doi.org/10.1007/S11661-021-06250-4>.

13 (49) Wu, D.; Kusada, K.; Nanba, Y.; Koyama, M.; Yamamoto, T.; Toriyama, T.;
14 Matsumura, S.; Seo, O.; Gueye, I.; Kim, J.; Rosantha Kumara, L. S.; Sakata, O.;
15 Kawaguchi, S.; Kubota, Y.; Kitagawa, H. Noble-Metal High-Entropy-Alloy
16 Nanoparticles: Atomic-Level Insight into the Electronic Structure. *J Am Chem Soc*
17 **2022**, 144 (8), 3365–3369. <https://doi.org/10.1021/JACS.1C13616>.

18 (50) Minamihara, H.; Kusada, K.; Yamamoto, T.; Toriyama, T.; Murakami, Y.;
19 Matsumura, S.; Kumara, L. S. R.; Sakata, O.; Kawaguchi, S.; Kubota, Y.; Seo, O.;
20 Yasuno, S.; Kitagawa, H. Continuous-Flow Chemical Synthesis for Sub-2 Nm
21 Ultra-Multielement Alloy Nanoparticles Consisting of Group IV to XV Elements.
22 *J Am Chem Soc* **2023**, 145 (31), 17136–17142.
23 <https://doi.org/10.1021/JACS.3C03713>.

24 (51) Tantardini, C.; Oganov, A. R. Thermochemical Electronegativities of the Elements.

Nature Communications 2021 12:1 **2021**, 12 (1), 1–9.
<https://doi.org/10.1038/s41467-021-22429-0>.

(52) Abrikosov, I. A.; Olovsson, W.; Johansson, B. Valence-Band Hybridization and Core Level Shifts in Random Ag-Pd Alloys. *Phys Rev Lett* **2001**, 87 (17), 176403.
<https://doi.org/10.1103/PhysRevLett.87.176403>.

(53) Chen, W.; Cao, J.; Yang, J.; Cao, Y.; Zhang, H.; Jiang, Z.; Zhang, J.; Qian, G.; Zhou, X.; Chen, D.; Yuan, W.; Duan, X. Molecular-Level Insights into the Electronic Effects in Platinum-Catalyzed Carbon Monoxide Oxidation. *Nature Communications* 2021 12:1 **2021**, 12 (1), 1–11. <https://doi.org/10.1038/s41467-021-27238-z>.

(54) Wu, D.; Kusada, K.; Yamamoto, T.; Toriyama, T.; Matsumura, S.; Gueye, I.; Seo, O.; Kim, J.; Hiroi, S.; Sakata, O.; Kawaguchi, S.; Kubota, Y.; Kitagawa, H. On the Electronic Structure and Hydrogen Evolution Reaction Activity of Platinum Group Metal-Based High-Entropy-Alloy Nanoparticles. *Chem Sci* **2020**, 11 (47), 12731–12736. <https://doi.org/10.1039/D0SC02351E>.

(55) Yuda, A.; Ashok, A.; Kumar, A. A Comprehensive and Critical Review on Recent Progress in Anode Catalyst for Methanol Oxidation Reaction. *Catalysis Reviews* **2022**, 64 (1), 126–228. <https://doi.org/10.1080/01614940.2020.1802811>.

(56) Mekazni, D. S.; Arán-Ais, R. M.; Ferre-Vilaplana, A.; Herrero, E. Why Methanol Electro-Oxidation on Platinum in Water Takes Place Only in the Presence of Adsorbed OH. *ACS Catal* **2022**, 12 (3), 1965–1970.
<https://doi.org/10.1021/ACSCATAL.1C05122>.

(57) Nandan, R.; Nanda, K. K. A Unique Approach to Designing Resilient Bi-Functional Nano-Electrocatalysts Based on Ultrafine Bimetallic Nanoparticles

- Dispersed in Carbon Nanospheres. *J Mater Chem A Mater* **2017**, 5 (21), 10544–10553. <https://doi.org/10.1039/C7TA02293J>.
- (58) Xue, S.; Deng, W.; Yang, F.; Yang, J.; Amiin, I. S.; He, D.; Tang, H.; Mu, S. Hexapod PtRuCu Nanocrystalline Alloy for Highly Efficient and Stable Methanol Oxidation. *ACS Catal* **2018**, 8 (8), 7578–7584. <https://doi.org/10.1021/ACSCATAL.8B00366>.
- (59) Kwon, S.; Ham, D. J.; Kim, T.; Kwon, Y.; Lee, S. G.; Cho, M. Active Methanol Oxidation Reaction by Enhanced CO Tolerance on Bimetallic Pt/Ir Electrocatalysts Using Electronic and Bifunctional Effects. *ACS Appl Mater Interfaces* **2018**, 10 (46), 39581–39589. <https://doi.org/10.1021/ACSAMI.8B09053>.
- (60) Huang, L.; Zhang, X.; Wang, Q.; Han, Y.; Fang, Y.; Dong, S. Shape-Control of Pt-Ru Nanocrystals: Tuning Surface Structure for Enhanced Electrocatalytic Methanol Oxidation. *J Am Chem Soc* **2018**, 140 (3), 1142–1147. <https://doi.org/10.1021/JACS.7B12353>.
- (61) Zhu, J.; Xia, L.; Yu, R.; Lu, R.; Li, J.; He, R.; Wu, Y.; Zhang, W.; Hong, X.; Chen, W.; Zhao, Y.; Zhou, L.; Mai, L.; Wang, Z. Ultrahigh Stable Methanol Oxidation Enabled by a High Hydroxyl Concentration on Pt Clusters/MXene Interfaces. *J Am Chem Soc* **2022**, 144 (34), 15529–15538. <https://doi.org/10.1021/JACS.2C03982>.
- (62) Nandan, R.; Nanda, K. K. Rational Geometrical Engineering of Palladium Sulfide Multi-Arm Nanostructures as a Superior Bi-Functional Electrocatalyst. *Nanoscale* **2017**, 9 (34), 12628–12636. <https://doi.org/10.1039/C7NR04733A>.
- (63) Nandan, R.; Goswami, G. K.; Nanda, K. K. Energy-Efficient Rational Designing of Multifunctional Nanocomposites by Preferential Anchoring of Metal Ions via Fermi Level Positioning of Carbon Nanostructures. *ACS Appl Mater Interfaces*

1 **2020**, *12* (48), 53749–53759. <https://doi.org/10.1021/ACSAMI.0C14858>.

2 (64) Iwasita, T. Electrocatalysis of Methanol Oxidation. *Electrochim Acta* **2002**, *47*
3 (22–23), 3663–3674. [https://doi.org/10.1016/S0013-4686\(02\)00336-5](https://doi.org/10.1016/S0013-4686(02)00336-5).

4 (65) Rus, E. D.; Wakabayashi, R. H.; Wang, H.; Abruña, H. D. Methanol Oxidation at
5 Platinum in Alkaline Media: A Study of the Effects of Hydroxide Concentration
6 and of Mass Transport. *ChemPhysChem* **2021**, *22* (13), 1397–1406.
7 <https://doi.org/10.1002/CPHC.202100087>.

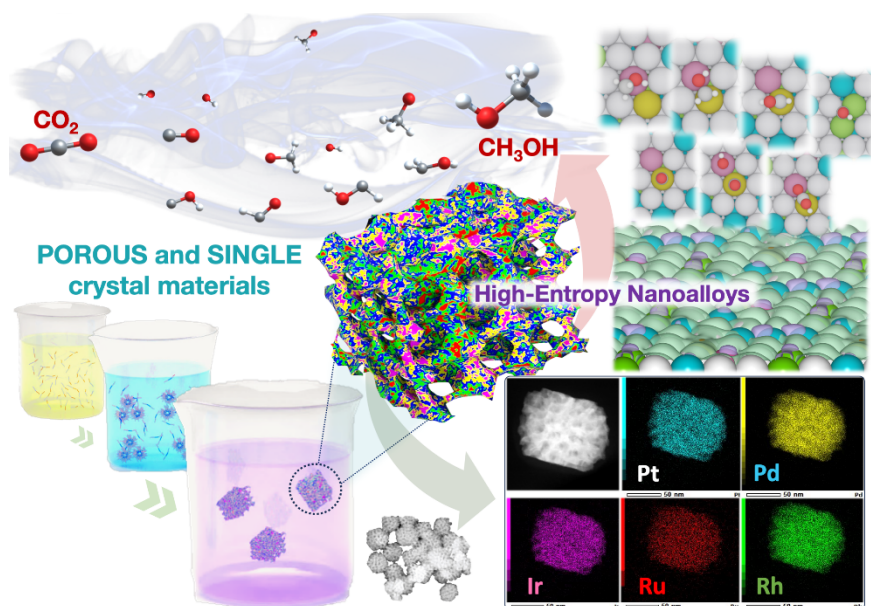
8 (66) Bagotzky, V. S.; Vassilyev, Y. B. Mechanism of Electro-Oxidation of Methanol on
9 the Platinum Electrode. *Electrochim Acta* **1967**, *12* (9), 1323–1343.
10 [https://doi.org/10.1016/0013-4686\(67\)80047-1](https://doi.org/10.1016/0013-4686(67)80047-1).

11 (67) Buck, R. P.; Griffith, L. R. Voltammetric and Chronopotentiometric Study of the
12 Anodic Oxidation of Methanol, Formaldehyde, and Formic Acid. *J Electrochem*
13 *Soc* **1962**, *109* (11), 1005. <https://doi.org/10.1149/1.2425226>.

14 (68) Dong, L.; Gari, R. R. S.; Li, Z.; Craig, M. M.; Hou, S. Graphene-Supported
15 Platinum and Platinum–Ruthenium Nanoparticles with High Electrocatalytic
16 Activity for Methanol and Ethanol Oxidation. *Carbon N Y* **2010**, *48* (3), 781–787.
17 <https://doi.org/10.1016/J.CARBON.2009.10.027>.

1

Table of Content Graphic



2

3 Designing of single-crystal porous high entropy nanoalloys for effective electro-oxidation
 4 of methanol.

5